INTERNATIONAL JOURNAL FOR NUMERICAL METHODS IN FLUIDS
Int. J. Numer. Meth. Fluids 2008; **58**:451–472
Published online 7 February 2008 in Wiley InterScience (www.interscience.wiley.com). DOI: 10.1002/fld.1752

Three-dimensional free surface flow simulation of segregating dense suspensions

F. Ilinca*,† and J.-F. Hétu

National Research Council, 75 de Mortagne, Boucherville, Que., Canada J4B 6Y4

SUMMARY

This paper presents a 3D numerical solution algorithm for the simulation of free surface flows of dense suspensions including particle migration phenomena. Segregation of the solid phase in processes such as powder injection molding and molding of semi-solid materials affects the rheology of the mixture and therefore the filling pattern. Segregation affects also the final properties and characteristics of such molded parts as a non-uniform particles distribution leads to non-uniform shrinkage, warpage and non-uniform mechanical properties. In this paper, particle migration is modeled using the diffusion flux model of Phillips *et al.* (*Phys. Fluids A* 1992; **4**:30–40) and is extended to address 3D mold filling problems. The solution algorithm is validated against flow problems for which experimental and numerical data are available: circular Couette flow, piston-driven flow and sudden contraction–expansion flow. The particle migration model is then used to simulate mold filling problems in which the piston movement in the sleeve is known to induce particle migration before the material enters the cavity. An arbitrary Lagrangian–Eulerian (ALE) formulation is developed and combined to a level-set front capturing method to simulate the piston movement and the evolution of the free surface in molding simulations. The ALE formulation is first compared with an Eulerian solution for the case of the piston-driven flow problem. The approach is then applied to injection molding problems to study the evolution of particle distributions during molding and in the final molded parts. Copyright © 2008 Crown in the right of Canada. Published by John Wiley & Sons, Ltd.

Received 16 August 2007; Revised 4 December 2007; Accepted 18 December 2007

KEY WORDS: dense suspensions; 3D modeling; finite elements; particle migration; diffusive flux model; free surface flow

1. INTRODUCTION

Experimental observation indicates that concentrated suspensions of spherical particles in a viscous fluid under non-homogeneous shear flow produce very non-uniform concentration distributions.

*Correspondence to: F. Ilinca, National Research Council, Industrial Materials Institute, 75 de Mortagne, Boucherville, Que., Canada J4B 6Y4.
†E-mail: florin.ilinca@cnrc-nrc.gc.ca

The ability to predict segregation of the solid phase in processes such as powder injection molding (PIM) is of special interest since such phenomenon affects the final properties and characteristics of the molded parts. Most PIM defects appear in the debinding and sintering stages but are often caused by filling problems and determined by non-uniform solid particle distribution within the solution. Inhomogeneous particle distribution affects the apparent viscosity and thus the flow during filling. This distribution may also affect the part deformation during sintering and consequently the final part geometry.

The general experimental observation is that particles migrate from regions of higher shear rate to regions of lower shear rate [1–3]. The migration takes place at particle Reynolds numbers small enough to conclude that inertial effects are negligible. Particle segregation may be caused by several mechanisms such as buoyancy, interparticle interactions and pressure gradient-induced migration. Dynamical simulations of many-particle systems that rigorously account for each fluid–particle and particle–particle interactions remain to computational expensive even for today's computers. Hence, simple numerical models representing the essential physics of the suspension would be very useful for flow simulations.

Various models have been proposed to describe the separation of the solid and fluid constituents in dense suspensions. In mixture models, each constituent is considered as a distinct specie of a mixture. The development of the mixture formulation is done by writing the conservation equations for each phase involved in the system. Two sets of momentum, mass and energy conservation equations are therefore written: one set for the liquid phase and one for the solid phase. Interaction between the two phases is taken into account by a momentum exchange term. The system of equations is closed by imposing mass conservation for the entire mixture: the sum of liquid and solid fractions equals the unity. The coupled fluid and solid equations can be solved directly [4, 5]; in such a case, the evaluation of the viscosity in the fluid and solid phases separately is needed [4]. To avoid the introduction of a solid phase *viscosity* and for computational efficiency reasons, the mixture model can be further simplified using phase mixture rules. By doing so, the two sets of conservation equations are reduced to one set of conservation equations into which the unknowns are the average mixture velocity, pressure and temperature [6, 7]. The local concentration of the mixture is computed using an additional phase concentration equation. In the case of semi-solid slurries, Pineau *et al.* [7] considered that the mixture behaves as a porous media and used a closure model based on the Darcy equation. This closure model implies that the separation mechanism is mainly driven by pressure gradients; the solid phase will increase in high-pressure regions such as stagnation points and before sudden contractions such as the gate. At some point, the Darcy closure model requires the determination of an effective permeability of the slurry as a function of solid fraction. This is done using the Carman–Kozeny equation. Manninen and Taivassalo [6] proposes a closure model based on particle drag. In this case, the relative velocity between the liquid and solid phases is dependent on the pressure gradient and also on the density difference between the liquid and solid phases. Because of the use of a pressure gradient closure model, mixture models are generally unable to predict the experimentally observed shear-induced particle migration [2].

Particle segregation can also be modeled using dense suspension models in which the segregation mechanism is driven by the shear rate. Conceptually, such models assume that particle–particle collision occurring in the suspension is the main driving force for phase separation. High-shear regions have a higher collision probability than low-shear regions; thus, based on probabilistic arguments, particles tend to migrate from the high-shear flow regions to the low-shear flow regions. Phillips *et al.* [8] introduced the diffusive flux model based on the concept of particle concentration

DOI: 10.1002/fld

diffusion. Experimental validation of the model for simple 1D or 2D problems is shown in References [9, 10]. The suspension balance model was first introduced by Nott and Brady [11], who introduced the concept of suspension '*temperature*'. Morris and Boulay [12] modified the model to take into account the effect of the normal stress difference, whereas Fang *et al.* [13] used a flow-aligned tensor to model the normal stress difference for both diffusive flux model and suspension balance model. Experimental validation of both diffusive flux and suspension balance models is shown in References [14, 15].

The objective of this work is to develop numerical simulation tools for the prediction of particle segregation in material forming processes such as PIM and molding of semi-solid materials. For this, a 3D numerical solution algorithm for the simulation of particle migration in dense suspensions was developed. The particle migration is modeled using the diffusion flux model proposed by Phillips *et al.* [8] and integrated into a 3D injection molding software [16].

The paper is organized as follows. First, the equations describing time-dependent laminar flow along with their boundary and initial conditions are presented in Section 2. The solid fraction equation describing particle segregation is presented. The arbitrary Lagrangian–Eulerian (ALE) formulation used to treat the piston movement in injection molding problems is also presented. The transient momentum, continuity, energy, particle concentration and front capturing equations are solved using linear finite elements. The solution algorithm and the finite element approach are described in Section 3. In Section 4, the approach is validated for flow problems for which experimental data are available: circular Couette flow, piston-driven flow and sudden contraction–expansion flow [9, 13, 17]. The ALE formulation is first compared with an Eulerian solution for the case of the piston-driven flow problem and used to solve the sudden contraction–expansion flow. The methodology is then applied in Section 5 for the prediction of particle segregation in an injection molding application. The paper ends with conclusions.

2. FLOW AND SEGREGATION EQUATIONS

2.1. Assumptions

The constitutive equations are given to represent the mechanical behavior of concentrated suspensions during the filling stage of the injection molding process. The main considerations behind the choice of model equations are described in this section.

The maximum pressure drop encountered during the filling of most PIM parts is about 10^6–10^7 Pa. Considering that the compressibility coefficient of polymer binders is of the order of $10^{-9}\,\mathrm{Pa}^{-1}$ and that the one of the mixture is even lower, one can conclude that compressibility effects can be neglected. The mixture is thus considered incompressible.

Polymer melts have a surface tension σ between 20 and 50 mN/m [18] and viscosities are of the order of 10^3 Pa s. Velocities at the interface are of the order of 0.05 m/s leading to a capillary number $Ca = \eta V/\sigma$ of the order of $O(10^3)$. Similar dimensional analysis leads to Reynolds numbers in the range of 10^{-4}–10^{-2}. One can conclude that viscous forces dominate and that both inertia and surface tensions can be neglected in the momentum equation. For the sake of generality and in order to be able to describe the flow of other types of concentrated suspensions (e.g. semi-solid metal injection molding) which may be characterized by higher flow velocity and lower viscosity, flow equations are expressed in a form that includes inertia.

2.2. Flow equations

The flow of incompressible fluids is described by the Navier–Stokes equations:

$$\rho\left(\frac{\partial \mathbf{u}}{\partial t}+\mathbf{u}_{\mathrm{c}}\cdot\nabla\mathbf{u}\right)=-\nabla p+\nabla\cdot(2\eta D_{ij}) \tag{1}$$

$$\nabla\cdot\mathbf{u}=0 \tag{2}$$

where t, $\mathbf{u}$, p, ρ and η denote time, velocity, pressure, density and viscosity, respectively, and $D_{ij}=(\partial u_i/\partial x_j+\partial u_j/\partial x_i)/2$ is the strain rate tensor. The convection velocity $\mathbf{u}_{\mathrm{c}}$ is equal to the fluid velocity $\mathbf{u}$ in an Eulerian frame reference, but depends on the mesh velocity $\mathbf{u}_{\mathrm{m}}$ in an ALE formulation:

$$\mathbf{u}_{\mathrm{c}}=\mathbf{u}-\mathbf{u}_{\mathrm{m}} \tag{3}$$

The apparent viscosity of the mixture η is computed as a function of the solid fraction ϕ using a modified Krieger–Dougherty model [19]:

$$\eta=\eta_{\mathrm{r}}\eta_{\mathrm{s}} \tag{4}$$

$$\eta_{\mathrm{r}}=(1-\overline{\phi})^{-1.82} \tag{5}$$

where η_{s} is the viscosity of the suspending fluid, η_{r} is the relative viscosity of the mixture with respect to that of the suspending fluid, and $\overline{\phi}$ denotes the normalized solid fraction, $\overline{\phi}=\phi/\phi_{\mathrm{m}}$; here, ϕ_{m} denotes the maximum solid fraction ($\phi_{\mathrm{m}}=0.68$).

2.3. Segregation model

In this work, we investigate only the case of incompressible mixtures having the same density for the solid particles and the liquid suspension. The segregation of solid particles is modeled by the diffusive flux model of Phillips *et al.* [8]. The solid fraction is, therefore, obtained by solving the transient advective–diffusive equation:

$$\frac{\partial\phi}{\partial t}+\mathbf{u}_{\mathrm{c}}\cdot\nabla\phi=-\nabla\cdot\mathbf{N} \tag{6}$$

where the diffusive flux $\mathbf{N}$ is given by

$$\mathbf{N}=\mathbf{N}_{\mathrm{c}}+\mathbf{N}_{\eta} \tag{7}$$

with $\mathbf{N}_{\mathrm{c}}$ describing the interaction caused by varying collision frequency and $\mathbf{N}_{\eta}$ describing the interaction caused by spatially varying viscosity:

$$\mathbf{N}_{\mathrm{c}}=-a^2\phi K_{\mathrm{c}}\nabla(\dot{\gamma}\phi) \tag{8}$$

$$\mathbf{N}_{\eta}=-a^2\phi^2\dot{\gamma}K_{\eta}\nabla(\ln\eta) \tag{9}$$

In the above equations a represents the radius of solid particles in the suspension, $\dot{\gamma}=\sqrt{2D_{ij}D_{ij}}$ is the shear rate invariant and K_{c} and K_{η} are model constants ($K_{\mathrm{c}}=0.41,\ K_{\eta}=0.62$).

2.4. Mold filling simulation

For mold filling applications in addition to solving for the flow equations, we have to track in time the position of the interface between the filling material and the air/void inside the cavity. Front tracking is done using a level-set method [20]. For this, a smooth function $F(x,t)$ is introduced such that a pre-determined value, F_c, represents the position of the interface. A value larger than F_c indicates a filled region, whereas in empty regions the front tracking function is smaller than F_c. The front tracking function is transported using the velocity field provided by the solution of the momentum–continuity equations:

$$\frac{\partial F}{\partial t}+\mathbf{u}_c\cdot\nabla F=0 \tag{10}$$

Fluid properties, such as density and viscosity, depend on whether the finite element corresponds to a filled, unfilled or partially filled volume. For example, the density ρ_K within the element K is computed using a linear interpolation between the mixture density ρ_m and the air density ρ_a, as

$$\rho_K=\rho_m\tilde{V}_{fk}+\rho_a(1-\tilde{V}_{fK}) \tag{11}$$

where $\tilde{V}_{fK}$ represents the portion of the element K that is filled by the mixture. A similar relationship is used for the computation of the viscosity. The filled volume fraction $\tilde{V}_{fK}$ is 1 in filled elements, 0 in unfilled elements and takes on values between 0 and 1 in partly filled elements. It represents the fraction of the element volume where the level-set function F is higher than F_c:

$$\tilde{V}_{fK}=\frac{1}{V_K}\int_{\Omega_K}H[F(x)-F_c]\,\mathrm{d}\Omega_K \tag{12}$$

where V_K is the volume of the element K and H is the Heaviside function.

As particle segregation during injection molding makes sense only in the filled part of the computational domain, the diffusive flux term in the solid fraction equation (6) is also pondered by the filled volume fraction. We solve, therefore, for

$$\frac{\partial\phi}{\partial t}+\mathbf{u}_c\cdot\nabla\phi=-\nabla\cdot(\tilde{V}_f\mathbf{N}) \tag{13}$$

2.5. Variable domain modeling

The ultimate goal of this research is the simulation of the segregation occurring in molding processes such as PIM and injection of semi-solid metals. In most injection molding applications, the material is pushed into the mold cavity by means of a plunger. To represent the flow behavior and segregation mechanism, we need to model the plunger advancement and hence consider changes in the computational domain. This is done by means of an ALE formulation with the geometrical change given by simple relationships depending on the plunger speed. The change of the computational domain in time is illustrated in Figure 1. The portion of the computational domain located between the initial plunger position $x=x_i$ and a fixed location $x=x_0$ (shown in darker gray scale in Figure 1) changes in time to account for the actual plunger position. At any given time t, this volume will be considered between the actual plunger location $x=x_i+u_pt$ and the

DOI: 10.1002/fld

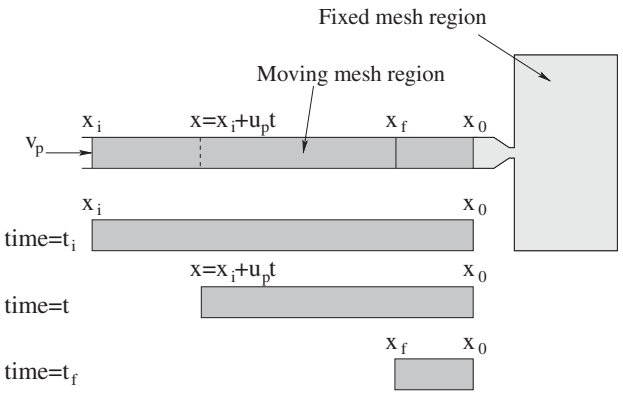

Figure 1. Computational domain change caused by plunger advancement during injection molding.

fixed location $x = x_0$. This part of the mesh is, therefore, simply compacted by the piston movement and no remeshing or insertion/removing of mesh elements is performed. Mesh deformation with time is given by the change of variables $x \to x^*$:

$$x^*(t) = \begin{cases} x + \dfrac{x_0 - x}{x_0 - x_i} u_\mathrm{p} t & \text{for } x \in [x_i, x_0] \\ x & \text{for } x \notin [x_i, x_0] \end{cases} \tag{14}$$

where u_p is the plunger velocity, x is the coordinate of a mesh point in the initial undeformed mesh (at $t = 0$) and x^* is the coordinate of the respective point in the deformed mesh. At the end of the filling ($t = t_f$), the plunger will be located at $x = x_f$ where $x_f = x_i + u_\mathrm{p} t_f$. As the mesh deforms, the ALE formulation of the conservation equations has to take into account for the mesh velocity given by

$$u_\mathrm{m} = \frac{\mathrm{d}x^*}{\mathrm{d}t} = \begin{cases} \dfrac{x_0 - x}{x_0 - x_i} u_\mathrm{p} & \text{for } x \in [x_i, x_0] \\ 0 & \text{for } x \notin [x_i, x_0] \end{cases} \tag{15}$$

The convection velocity is then computed using Equation (3).

2.6. Boundary conditions

The problem definition is completed by imposing boundary conditions. Boundary conditions for the validation cases are detailed in the Section 4. For the injection molding application, no-slip boundary conditions are imposed on the cavity walls filled by the suspension, whereas on the unfilled part, a free boundary condition allows for the formation of the typical fountain flow. The solid fraction is set to an initial value and then a zero solid fraction flux is imposed on the boundary. This will ensure that the total particle concentration remains constant inside the computational domain.

3. FINITE ELEMENT SOLUTION

Model equations are discretized in time using a first-order implicit Euler scheme. Linear continuous shape functions are used for all variables. At each time step, the global system of equations is solved in a partly segregated manner. The solution algorithm solves separately the systems of equations as follows:

For time smaller than the end time:

1. Solve the incompressible momentum-continuity equations ($\mathbf{u}-p$).
2. Solve the solid fraction equation (ϕ).
3. Solve the energy equation (T) if present (non-isothermal flow problems).
4. Solve the front tracking equation F for injection molding problems.

Check convergence. If converged goto the next time step, otherwise repeat steps 1 to 4.

Steps 1–4 are solved using the last known values of the dependent variables and iterations are made to obtain converged solutions of the coupled system of equations. The finite element formulations of the equations are discussed hereafter.

3.1. Flow equations

The Navier–Stokes equations (1) and (2) are solved using a Galerkin least-squares (GLS) method [21]. This method contains an additional pressure stabilization term compared with the standard Galerkin method. In such a way, the use of linear elements for both the velocity and pressure is permitted. The GLS variational formulation of the momentum–continuity equations is

$$\int_\Omega \rho\left(\frac{\partial \mathbf{u}}{\partial t}+\mathbf{u}_c\cdot\nabla\mathbf{u}\right)\mathbf{v}\,\mathrm{d}\Omega+\int_\Omega 2\eta D_{ij}(\mathbf{u}):D_{ij}(\mathbf{v})\,\mathrm{d}\Omega-\int_\Omega p\nabla\cdot\mathbf{v}\,\mathrm{d}\Omega+\int_\Omega \nabla\cdot\mathbf{u}q\,\mathrm{d}\Omega$$
$$+\sum_K\int_{\Omega_K}\left\{\rho\left(\frac{\partial \mathbf{u}}{\partial t}+\mathbf{u}_c\cdot\nabla\mathbf{u}\right)+\nabla p-\nabla\cdot[2\eta D_{ij}(\mathbf{u})]\right\}\cdot\tau_u\{\rho\mathbf{u}_c\cdot\nabla\mathbf{v}+\nabla q\}\,\mathrm{d}\Omega_K=0 \quad (16)$$

where $\mathbf{v}$ and q are the velocity and pressure test functions, respectively. The stabilization parameter τ_u is defined as [22, 23]

$$\tau_u=\left[\left(\frac{2\rho}{\Delta t}\right)^2+\left(\frac{2\rho|\mathbf{u}_c|}{h_K}\right)^2+\left(\frac{4\eta}{m_k h_K^2}\right)^2\right]^{-1/2} \quad (17)$$

Here, Δt is the time step, h_K is the size of the element K and m_k is a coefficient set to $\frac{1}{3}$ for linear elements (see [21, 22]).

For PIM applications, the flow is at low Reynolds number and the transient and convective terms are negligible. Hence, the stabilized form of the momentum-continuity equations is

$$\int_\Omega 2\eta D_{ij}(\mathbf{u}):D_{ij}(\mathbf{v})\,\mathrm{d}\Omega-\int_\Omega p\nabla\cdot\mathbf{v}\,\mathrm{d}\Omega+\int_\Omega \nabla\cdot\mathbf{u}q\,\mathrm{d}\Omega$$
$$+\sum_K\int_{\Omega_K}\{\nabla p-\nabla\cdot[2\eta D_{ij}(\mathbf{u})]\}\cdot\tau_u\nabla q\,\mathrm{d}\Omega_K=0 \quad (18)$$

DOI: 10.1002/fld

with the stabilization parameter τ_u given by

$$\tau_u = \frac{m_k h_K^2}{4\eta} \tag{19}$$

3.2. Solid fraction equation

The solid fraction equation is solved by a streamline upwind Petrov–Galerkin (SUPG) method. SUPG provides smooth solutions when the convective part of the equation is dominant, as is in the present case. The finite element formulation, once the diffusive flux term is integrated by parts, is as follows:

$$\int_{\Omega_f} \left(\frac{\partial \phi}{\partial t} + \mathbf{u}_c \cdot \nabla \phi \right) w \, \mathrm{d}\Omega - \int_{\Omega_f} \tilde{V}_f (\mathbf{N}_c + \mathbf{N}_\eta) \cdot \nabla w \, \mathrm{d}\Omega$$
$$+ \sum_{K \in \Omega_f} \int_{\Omega_K} \left(\frac{\partial \phi}{\partial t} + \mathbf{u}_c \cdot \nabla \phi \right) \tau_\phi \mathbf{u}_c \cdot \nabla w \, \mathrm{d}\Omega_K = - \int_{\partial \Omega_f} \tilde{V}_f (\mathbf{N}_c + \mathbf{N}_\eta) \cdot \hat{\mathbf{n}} w \, \mathrm{d}\Gamma \tag{20}$$

The integrals over Ω_f in the first row together with the right-hand side term represent the standard Galerkin formulation with the diffusive flux integrated by parts. The sum of integrals over the element interiors represents the SUPG stabilization term. The solid fraction equation is solved only on the region Ω_f of the computational domain composed by filled and partly filled elements. In the rest of the computational domain, the solid fraction is set equal to the initial value. The boundary term in the right-hand side of (20) represents the solid fraction flux across the boundary. As there is no transfer of either liquid or solid material across mold walls and the mixture/air interface, this flux is taken zero. As the sum of diffusion terms for all test functions is zero and the diffusion flux across boundaries is also zero, this finite element formulation enforces the conservation of the total solid content within the filled region of the computational domain.

Remark that by integrating by parts the diffusive flux term, we avoid differentiation of the flux terms $\mathbf{N}_c$ and $\mathbf{N}_\eta$. However, we still have to deal with the derivative of the shear rate in the expression of $\mathbf{N}_c$ and with the derivative of the viscosity in that of $\mathbf{N}_\eta$:

$$\mathbf{N}_c = -a^2 \phi K_c (\dot{\gamma} \nabla \phi + \phi \nabla \dot{\gamma}) \tag{21}$$

$$\mathbf{N}_\eta = -a^2 \phi^2 \dot{\gamma} K_\eta \frac{\nabla \eta}{\eta} \tag{22}$$

The viscosity depends on the solid fraction and its derivative is computed as

$$\nabla \eta = \frac{\mathrm{d}\eta}{\mathrm{d}\phi} \nabla \phi \tag{23}$$

The derivative of the shear rate, however, is not as straightforward as that of the viscosity. The velocity is interpolated using piecewise linear elements. Therefore, the shear rate $\dot{\gamma}$ is constant inside mesh elements and undetermined at the boundary between elements. To compute the diffusive flux term, we perform a projection of the finite element shear rate into the space of linear continuous interpolation functions. This is done by a local projection method [24, 25]. Therefore, in the computation of the diffusive fluxes $\mathbf{N}_c$ and $\mathbf{N}_\eta$, the finite element shear rate $\dot{\gamma}$ is replaced by a projected one, interpolated using the same linear continuous functions as for the other variables.

DOI: 10.1002/fld

The apparent diffusion coefficient corresponding to the diffusion flux $\mathbf{N}$ is given by

$$k_\phi = a^2 \phi \dot{\gamma} K_c \left(1 + \frac{K_\eta}{K_c} \frac{\phi}{\eta} \frac{d\eta}{d\phi}\right) \tag{24}$$

and the stabilization parameter τ_ϕ is therefore computed as

$$\tau_\phi = \left[\left(\frac{2}{\Delta t}\right)^2 + \left(\frac{2|\mathbf{u}_c|}{h_K}\right)^2 + \left(\frac{4k_\phi}{m_k h_K^2}\right)^2 \right]^{-1/2} \tag{25}$$

3.3. Front tracking equation

The front tracking equation is discretized using an SUPG finite element method. The variational formulation is given by

$$\int_\Omega \left(\frac{\partial F}{\partial t} + \mathbf{u}_c \cdot \nabla F\right) v \, d\Omega + \sum_K \int_{\Omega_K} \left(\frac{\partial F}{\partial t} + \mathbf{u}_c \cdot \nabla F\right) \tau_F (\mathbf{u} \cdot \nabla v) \, d\Omega_K = 0 \tag{26}$$

In the absence of diffusion, the stabilization coefficient τ_F is defined as

$$\tau_F = \left[\left(\frac{2}{\Delta t}\right)^2 + \left(\frac{2|\mathbf{u}_c|}{h_K}\right)^2 \right]^{-1/2} \tag{27}$$

The front tracking function is discretized using linear elements and reinitialized after each time step to ensure mass conservation of the injected material [26].

4. VALIDATION

In this section, the solution algorithm is validated on cases for which both experimental and numerical data are available: circular Couette flow, piston-driven flow and sudden contraction–expansion flow [9, 13].

4.1. Circular Couette flow

This flow problem was the object of an experimental study by Abbott *et al.* [27] and reinvestigated both numerically and experimentally by Tetlow *et al.* [10]. The experimental apparatus has the inner rod (R_i) of 0.64 cm and the inner radius of the outer tube (R_o) of 2.38 cm (see Figure 2).

The flow is axi-symmetric and can also be solved using the model equations expressed in cylindrical coordinates. Because the variables depend only along the tube radius, a simplified 1D problem can be obtained. The only variables to be solved are the circumferential velocity u_θ and the solid fraction ϕ. The axial and radial velocity components are zero, whereas the pressure is

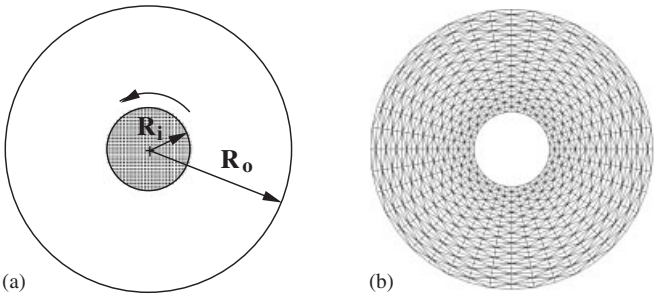

Figure 2. Circular Couette flow problem: (a) problem definition and (b) mesh with 20 elements in radial direction.

constant. The 1D problem for the circular Couette flow can be expressed as

$$\frac{1}{r^2}\frac{\partial}{\partial r}\left[\eta r^3 \frac{\partial}{\partial r}\left(\frac{u_\theta}{r}\right)\right]=0 \tag{28}$$

$$\frac{\partial \phi}{\partial t}=\frac{1}{r}\frac{\partial}{\partial r}\left[ra^2\phi K_c\frac{\partial}{\partial r}(\dot{\gamma}\phi)\right]+\frac{1}{r}\frac{\partial}{\partial r}\left[ra^2\phi^2\dot{\gamma}K_c\frac{\partial}{\partial r}(\ln\eta)\right] \tag{29}$$

The problem is solved using both the 3D solution algorithm and the 1D model equations. This way, the 3D algorithm is validated using the 1D solution as a reference. Then the predictive capability of the model is quantified by comparing the numerical results with the experimental data.

The initial particle concentration ϕ_0 is taken constant. Simulations were first carried out to verify the transient behavior of the solution. The particles diameter is 128 μm, the initial solid fraction is 0.5 and the inner rod rotates at 60 rpm. The suspension viscosity is 2.1 Pa s. As can be seen from Figure 3, the 1D (discontinuous lines) and 3D (continuous lines) solutions are almost identical. The numerical solution recovers well the behavior observed in the experiment; the particle concentration decreases in the vicinity of the inner rod and increases close to the outer cylinder. The model seems to predict a faster decay rate of the particle concentration near the inner rod when compared with the experiment. The steady-state particle distribution for various initial solid fractions is shown in Figure 4. Only the 3D, solution is compared with the experiment here. For the steady-state simulations, the particles diameter is 1497 μm and the inner rod rotates at 60 rpm. At steady-state the solution does not depend on the particle size but only on the initial value of the particle concentration. The numerical results are in good agreement with the experimental data of Tetlow *et al.* [10]. In Figure 5, the 1D and 3D solutions are compared for different mesh densities and for an initial solid fraction of 0.5. As can be seen, the two solution methods result in similar predictions and the effect of the mesh size is negligible. The only small discrepancy is observed for the solution on the coarser mesh at the inner rod surface and is explained by the fact that in the 1D case a second-order accurate derivative of the shear rate is used at the boundary, whereas in the 3D solution the derivative at the boundary is first-order accurate.

4.2. Piston-driven flow

This validation case consists of displacing a fixed volume of suspension down a pipe by means of a piston. The material exhibits a similar behavior in injection molding where the suspension

DOI: 10.1002/fld

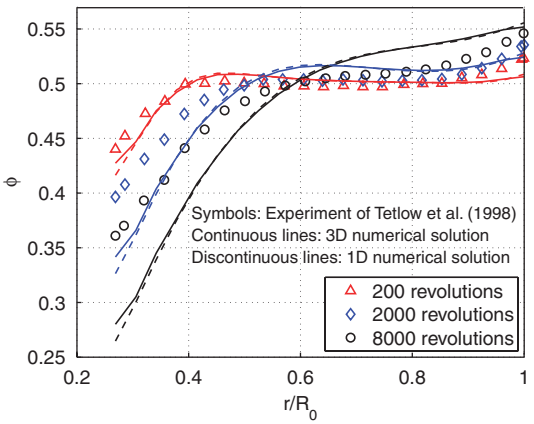

Figure 3. Transient Couette flow: comparison of model prediction with experimental particle concentration profiles of Tetlow *et al.* [10].

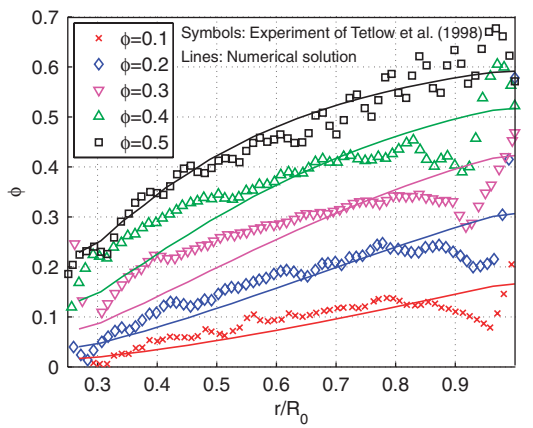

Figure 4. Comparison of steady-state prediction with experimental particle concentration profiles of Tetlow *et al.* [10].

pushed by a piston forms a free surface. The uniformity of the suspension downstream of the piston will then affect the distribution of particles inside the molded part. An experimental study of this problem was performed by Subia *et al.* [9]. The piston radius is 2.54 cm and the pipe was filled with material on a length of 30 cm. In the initial state the suspension is homogeneous and contains 50% of spherical particles having 3178 μm in diameter. The piston moves from left to right at a speed of 0.0625 cm/s, whereas the pipe was held stationary as shown in Figure 6.

A first computation was carried out on a fixed mesh by considering that the pipe moved from right to the left and the pistons were maintained fixed. This way a reference solution was obtained using an Eulerian approach. The mesh for this simulation has 52 569 nodes and is formed by 257 280 tetrahedral elements. The mesh and flow pattern along the symmetry plane after the piston was displaced with 15 piston diameters is shown in Figure 7. Particle segregation for different

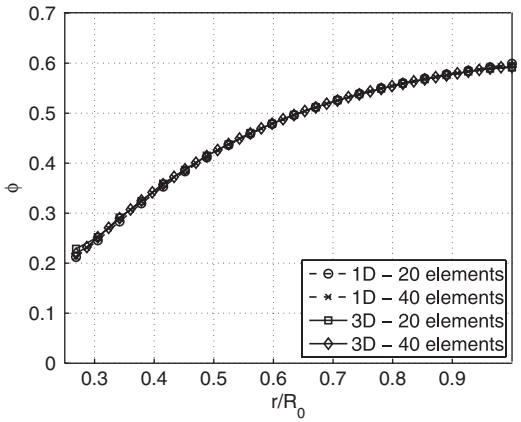

Figure 5. Circular Couette flow: effect of mesh size on the 1D and 3D solutions for $\phi_0 = 0.5$.

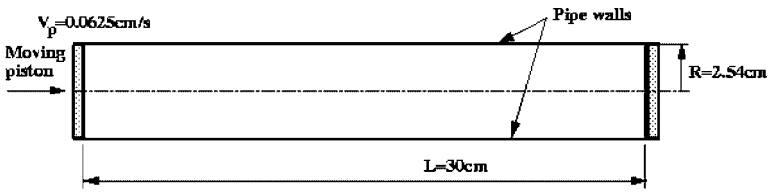

Figure 6. Problem definition for piston-driven flow problem.

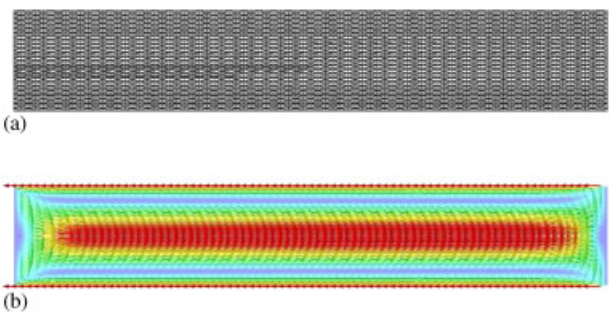

Figure 7. Piston-driven flow problem: solution for Eulerian approach: (a) finite element mesh and (b) velocity distribution after 15 piston diameters ($15D$).

positions of the piston is shown in Figure 8. The solid fraction decreases in front of the piston pushing the suspension and is higher in the second half of the domain along the pipe axis. This is in agreement with experimental observation [9].

The mean solid fraction on sections normal to the pipe axis was computed and plotted along the pipe axis in Figure 9. The results are compared with experimental data collected after the piston was displaced with 5 piston diameters. The numerical solution recovers correctly the segregation

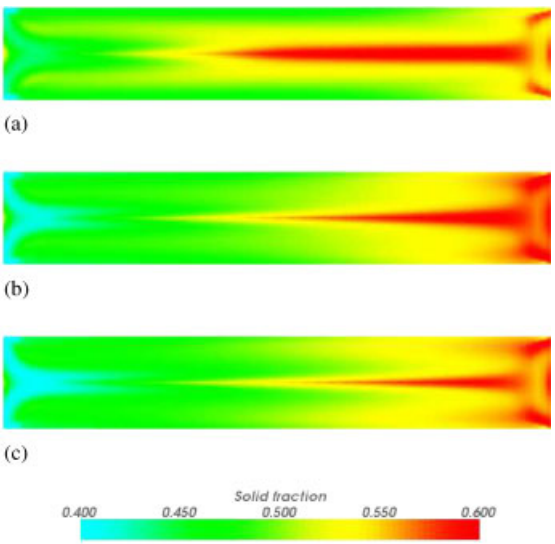

Figure 8. Distribution of solid fraction for various piston displacements (Eulerian approach): (a) after $5D$; (b) after $10D$; and (c) after $15D$.

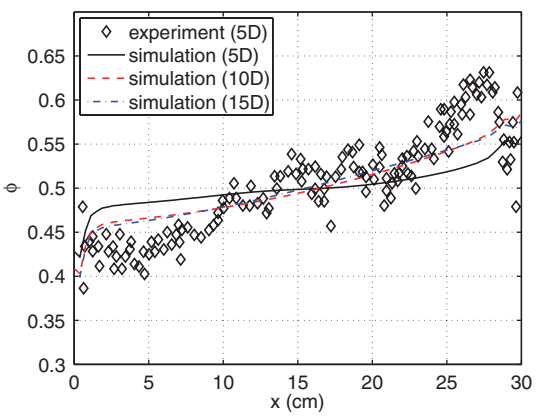

Figure 9. Mean solid fraction along the tube axis using an Eulerian approach (experimental data from Subia *et al.* [9]).

behavior, but slightly underestimates the change in the solid fraction. However, the agreement with previously published numerical results [13] is very good. Simulation indicates that the segregation in front of a moving piston evolves quite rapidly and that an almost developed flow is attained after a $10D$ piston displacement.

This problem describes well the behavior of the material in front of the plunger during injection molding. However, simulation of the piston movement in material processing would not be possible in an Eulerian frame of reference, since the model includes both the moving piston and stationary parts as the mold cavity. Therefore, the more general ALE formulation described in Section 2.5

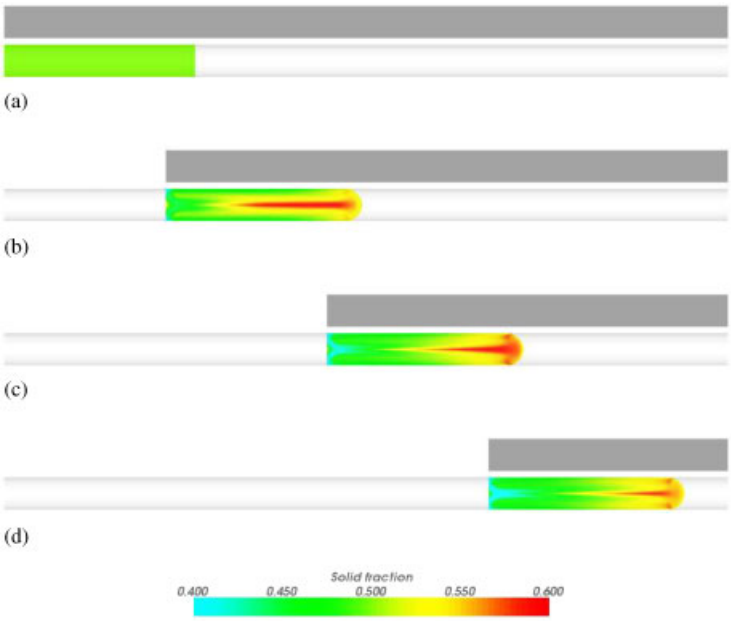

Figure 10. Computational domain and distribution of solid fraction for various piston displacements (ALE formulation): (a) initial solution; (b) after $5D$; (c) after $10D$; and (d) after $15D$.

needs to be considered. The ALE simulation was carried out on a mesh with 104 489 nodes and 499 200 tetrahedral elements. There were 16 elements in radial direction, 48 elements along the piston circumference and 160 elements along the pipe axis. However, as only part of the domain is filled and the mesh is compacted by the movement of the piston, the number of filled elements along the pipe axis was only 41 for the initial solution and increased to 127 after a $15D$ displacement. Results using the ALE formulation for the piston-driven flow with a free surface are shown in Figures 10 and 11. Figure 10 illustrates the solid fraction distribution in a cross-section along the pipe axis. It also shows the change in the computational domain (gray rectangles) and the form of the free surface on the right-hand end of the filled region. The results are very close to those given by the Eulerian approach (Figure 9). Small differences are observed at the right end of the computational domain, where a non-planar free surface is present in the ALE solution and a flat no-slip surface is present in the Eulerian case. The agreement between the two sets of computations indicates that the ALE approach performs well and can be used for injection molding applications.

A detail of the solution in the free surface region is compared with the Eulerian solution in Figure 12. As can be seen, both solutions indicate a buildup of particles at the right end of the filled domain, which corresponds to the piston surface in the Eulerian approach and, respectively, to the flow front in the case of the free surface computation. The behavior of the solution is similar in the two cases, with a band of higher solid fraction in the center of the pipe, and higher particle concentration close to the wall in the vicinity of the free surface.

The particle migration towards the center of the flow through a tube and the buildup of higher solid particle concentration in the vicinity of the free surface are well documented by experimental observation [1, 28, 29]. Tang *et al.* [30] associated the observed instability of the fluid/air interface

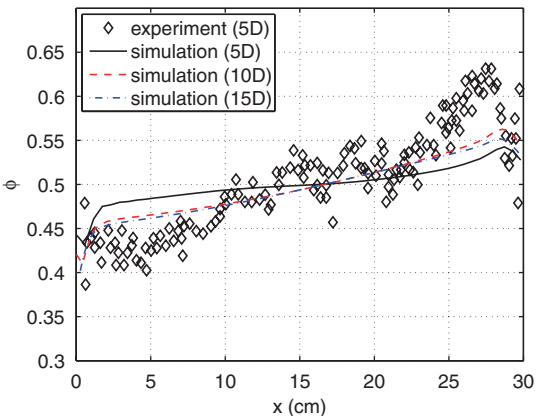

Figure 11. Mean solid fraction along the tube axis using an ALE approach (experimental data from Subia *et al.* [9]).

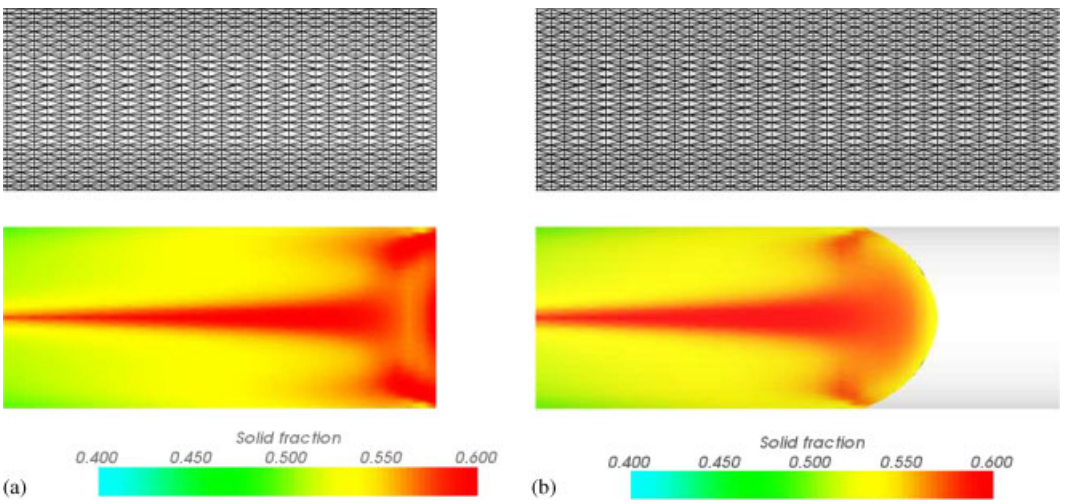

Figure 12. Detail of the mesh and solution at the free surface: (a) Eulerian approach and (b) ALE formulation.

under specific conditions to the particle accretion in the meniscus region. In the present piston-driven flow, the particle concentration is significantly higher in the right-hand side of the tube (downward with reference to the flow direction). To illustrate this phenomenon, we divided the flow domain shown in Figure 6 into two equal size sub-domains: one for $x<L/2$ and the other for $x>L/2$ ($x=L/2$ denotes the middle of the fluid region). One can observe that the region near the center of the pipe has higher flow rate and also higher particle concentration. Thus, even if the net flow exchange between the left and right sub-domains is zero, there is a non-zero particle flux across the surface between the two sub-domains at $x=L/2$ as shown in Figure 13(a). The mean volumetric particle concentration in the left and right sub-domains is shown in Figure 13(b). A

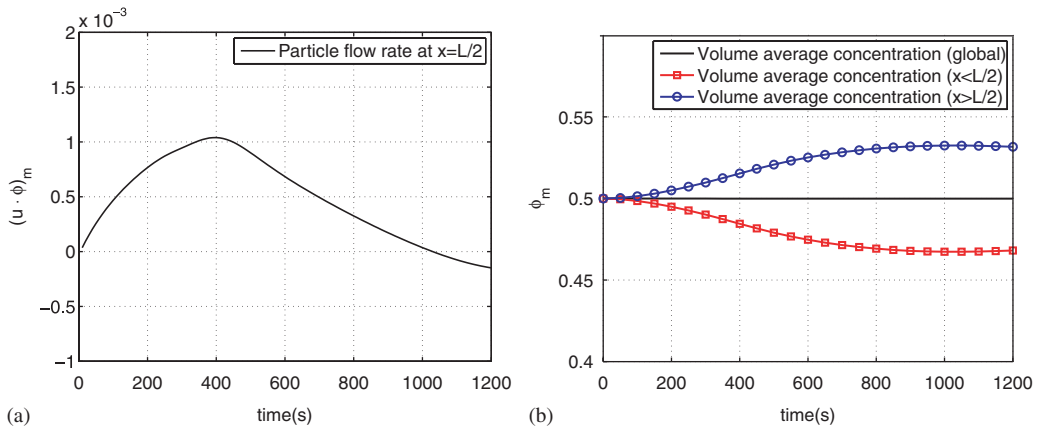

Figure 13. Particle migration from one side to the other of the flow domain: (a) net particle flux across $x = L/2$ and (b) mean volumetric particle concentration.

positive particle flux indicates that more particles are transported from the left towards the right sub-domain than in the opposite direction. Therefore, the mean volumetric particle concentration increases in the right side. This happens until $t = 1000$ s, from which point the left/right particle migration reverses and the net particle flux is from the right towards the left side.

4.3. Sudden contraction–expansion flow

In this test case, the suspension is pushed by a piston from a reservoir pipe into a smaller diameter pipe and then into another larger catch pipe. The flow conditions follow those of the experimental study by Altobelli *et al.* [31]. The reservoir pipe and the catch pipe have a diameter of 5.08 cm, whereas the smaller pipe has an inner diameter of 1.27 cm. The smaller diameter pipe is 38 cm long. Initially 30 cm of the reservoir pipe, the entire smaller diameter pipe and 4 cm of the catch pipe were filled. The plunger was displaced at a constant velocity of 0.0625 cm/s, resulting in a mean velocity of 1 cm/s in the smaller pipe. The solid particles in the suspension were 50% by volume with a mean particle diameter of 675 μm.

The numerical solution was obtained using the ALE formulation. The mesh changes with time in both larger diameter pipes, but remains fixed in the smaller diameter pipe. The initial computational mesh and solid fraction and those after the piston moves 2, 4 and 6, respectively, larger section diameters are shown in Figure 14. The mean solid fraction along the pipe axis is shown in Figure 15. Several observations can be drawn from these results. First, we remark that the solid fraction decreases at the surface of the moving piston, observation made also in the case of the piston-driven flow. Second, we observe a sharp increase in the solid fraction just prior to the 4:1 contraction ($x = 0$ cm). The solid fraction decreases then rapidly and reaches smaller values along the smaller diameter pipe. Third, we remark that at the 1:4 expansion, $x = 38$ cm, the solid fraction decreases before the section change and increases on a very small region after the expansion. In the catch pipe, $x > 38$ cm, the solid fraction is initially smaller than the mean value of 0.5, but increases towards the end of the pipe.

DOI: 10.1002/fld

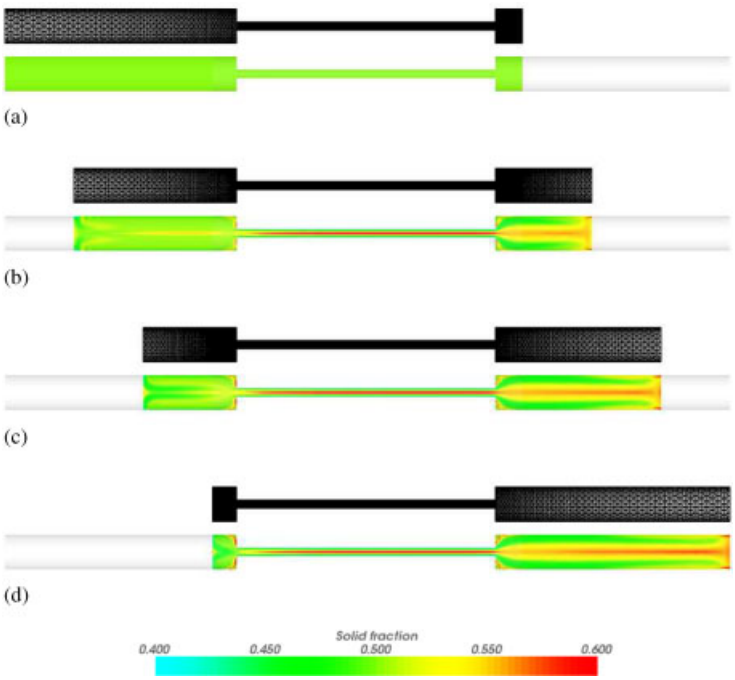

Figure 14. Contraction–expansion flow: computational mesh and distribution of solid fraction for various piston displacements: (a) initial solution; (b) after $2D$; (c) after $4D$; and (d) after $6D$.

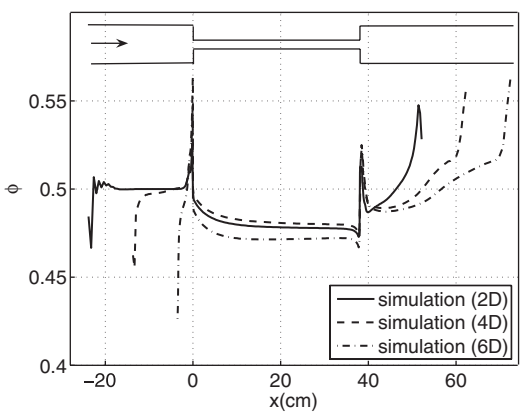

Figure 15. Sudden contraction–expansion flow: mean solid fraction along the pipe axis using an ALE approach.

There is an apparent contradiction when analyzing the numerical solution in Figure 15. The flow passes through the smaller diameter pipe having a smaller particle concentration, but higher particle concentration is obtained in the catch pipe. A closer look at this behavior is needed.

Remark first that the particle exchange between two regions is determined by the flow average concentration, which may be different from the volume average concentration. In fact, as the higher flow rate around the center of the pipe also has a higher particle concentration, it results that the flow average concentration in such regions is higher than the local volume average concentration. To illustrate this effect, the computational domain was separated into two sub-domains by the surface normal to the pipe axis, located at $x/L=0.5$ (center of the smaller diameter pipe). The mean particle concentration in the left- and right-hand side sub-domains was computed as well as the flow average particle concentration on the interface $x/L=0.5$. Their variation is plotted against time in Figure 16. The following relationships were used:

- The volume average concentration in a domain Ω is given by

$$\phi_{\mathrm{m}}=\frac{\int_{\Omega}\phi\,\mathrm{d}\Omega}{\int_{\Omega}\mathrm{d}\Omega} \tag{30}$$

- The flow average concentration across a surface Γ is given by

$$\phi_{\mathrm{m}}=\frac{\int_{\Gamma}\mathbf{u}\cdot\hat{\mathbf{n}}\phi\,\mathrm{d}\Omega}{\int_{\Gamma}\mathbf{u}\cdot\hat{\mathbf{n}}\,\mathrm{d}\Omega} \tag{31}$$

where $\hat{\mathbf{n}}$ is the unit vector normal to Γ. The average concentration in the left-hand side sub-domain ($x/L<0.5$) is shown by the line with square symbols, the one on the right-hand side is shown by the line with circles, whereas the average particle concentration in the whole domain is shown with a simple continuous line. As expected, the mean particle concentration in the complete domain remains constant. The discontinuous line corresponds to the flow average concentration across $x/L=0.5$. The mean particle concentration in a given volume increases when the net flow average concentration across its boundaries is higher than the concentration inside the volume. It is exactly what can be observed in Figure 16. The average concentration in the right-hand side sub-domain ($x/L>0.5$) increases whenever the flow average concentration on its boundary is higher than itself and decreases when it is lower than itself. Similar observations can be made for the average

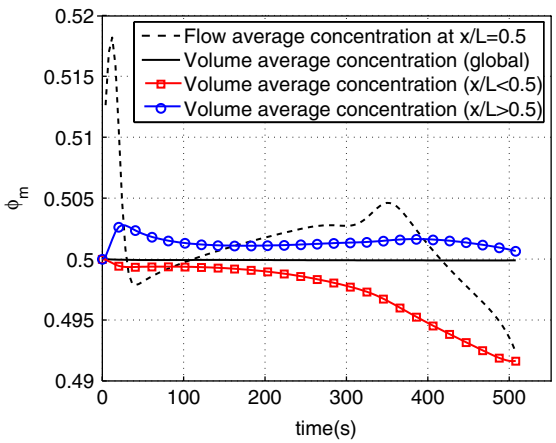

Figure 16. Particle concentration on the left- and right-hand side of the center of smaller diameter pipe.

DOI: 10.1002/fld

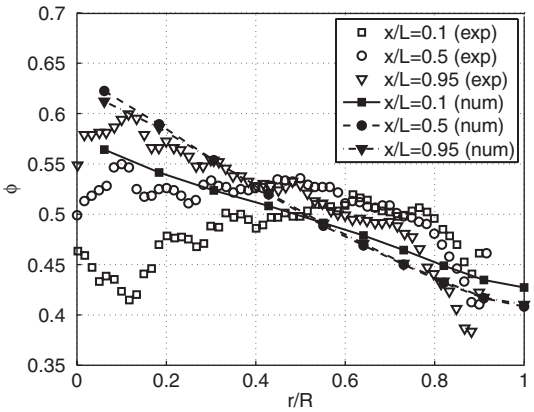

Figure 17. Solid fraction in radial direction at various locations along the smaller diameter pipe.

concentration in the left-hand side sub-domain, but in this case we are in the presence of an outward particle flow and the effect is in opposite direction. The average concentration increases whenever the flow average concentration at $x/L=0.5$ is lower than itself and decreases when it is higher than itself. Note that this may even cause the two average concentrations to decrease at the same time as is the case towards the end of the simulation (the total average concentration still remains constant).

The solid fraction distribution in radial direction at various locations along the smaller diameter pipe is compared with the experimental data of Altobelli *et al.* [31] in Figure 17. Results are plotted for $x/L=0.1$, 0.5 and 0.95, where L denotes the length of the smaller diameter pipe and x is the coordinate along the pipe measured in the sense of the flow (from the contraction, $x=0$, towards the expansion, $x=L$). The results indicate that the solid fraction is larger near the axis of the pipe and decreases close to the pipe wall. We also remark that the segregation is more pronounced at $x/L=0.5$ and 0.95 than at the entry of the smaller diameter pipe. These observations agree well with the experimental findings of Altobelli *et al.* [31].

5. MOLD FILLING APPLICATION

In this application, the ALE formulation is used to solve the injection molding of a rectangular plate. The plate is 8 by 6 cm and has 4 mm thickness. The filling piston has a radius of 1 cm and its displacement is 13.2 cm. Filling of the plate is made through a circular gate with a radius of 2 mm. The suspension contains particles of 100 μm in diameter and the initial solid fraction is uniform at 50%. Complete filling of the plate takes 9.7 s. The filling pattern and the solid fraction distribution are shown in Figure 18 after 1.9, 4.2, 7.1 and 9.7 s, respectively. The figure shows a cut along the symmetry plane parallel to the longest side of the plate in order to see the solid fraction distribution inside the part. The images show both the complete domain, where the displacement of the piston during the filling is clearly seen, and details of the flow inside the plate. Segregation of solid particles is apparent inside the pipe as previously observed for the piston-driven flow case.

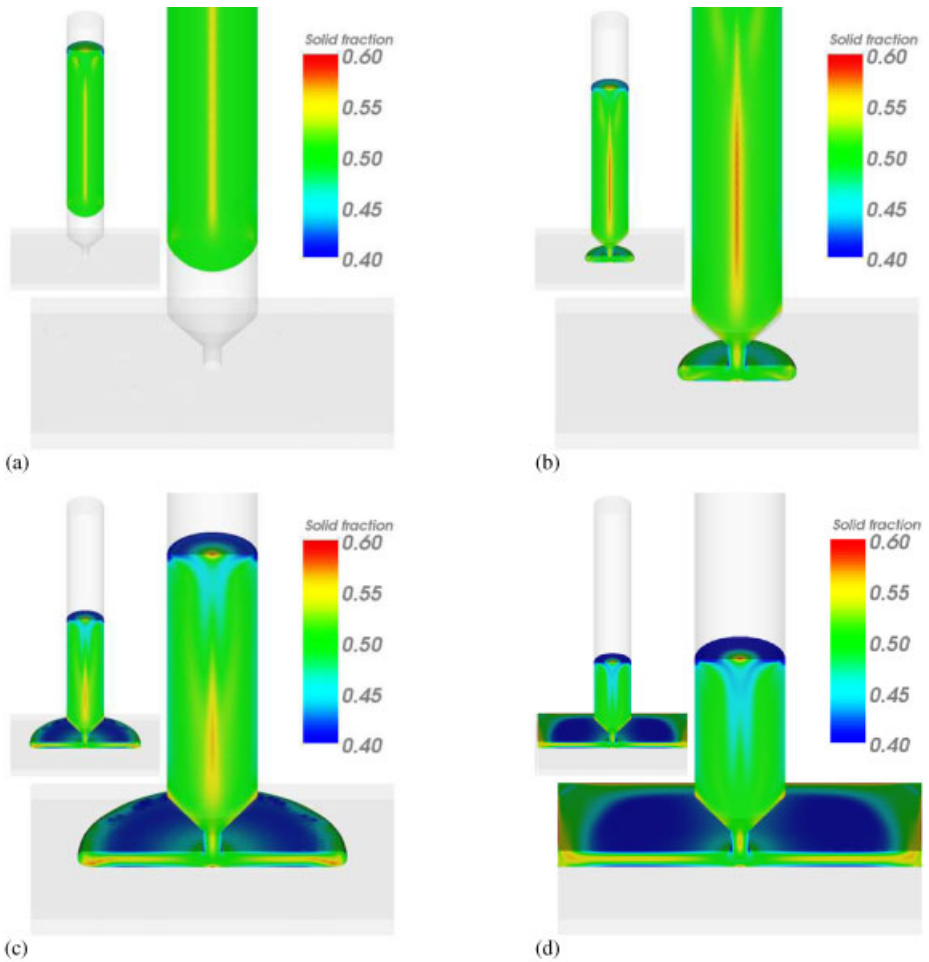

Figure 18. Distribution of solid fraction for the injection of a plate: (a) $t = 1.9$ s; (b) $t = 4.2$ s; (c) $t = 7.1$ s; and (d) $t = 9.7$ s.

This causes the material to enter the gate with a non-uniform solid fraction. Additional segregation is observed inside the gate where shear rates are highest. The molded part has higher solid fraction in the mid-plane and on the boundaries of the plate (far from the gate) and lower solid fraction on the upper and lower surfaces.

The particle concentration at the end of the filling time for various locations inside the gate and along the plate is shown in Figure 19. Figure 19(a) shows the solution at gate inlet and outlet, as well as mid-way between the two locations. The gate length is 5 mm. Note that particle concentration increases near the gate axis, where velocities are higher. At the exit from the gate, the particle concentration decreases significantly near the walls. Particle distribution across the thickness of the plate at 1, 2 and 3 cm, respectively, from the gate (in the center plane parallel

DOI: 10.1002/fld

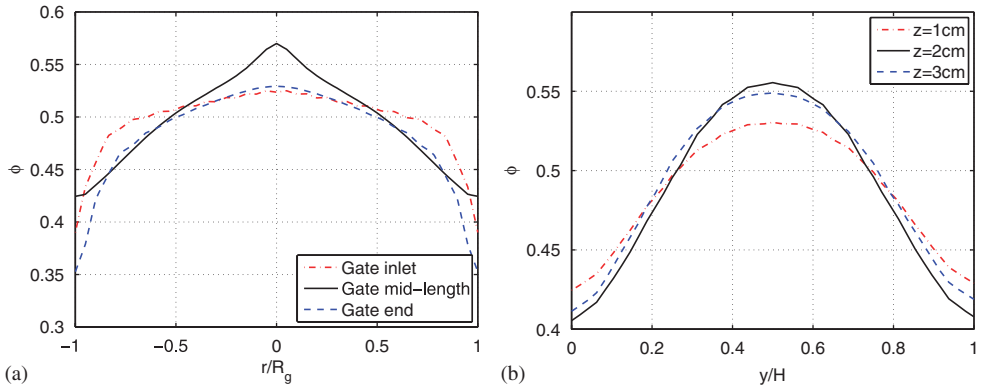

Figure 19. Distribution of solid fraction for the injection of a plate: (a) concentration inside the gate and (b) concentration across the thickness of the plate.

to the longest side) are shown in Figure 19(b). In all sections, the concentration is higher in the center and lower at the walls.

6. CONCLUSION

In this paper, a 3D finite element algorithm is presented to model and simulate free surface flows of dense suspensions. The segregation of solid particles is described by a diffusive flux model. Validation cases show a good agreement with experimental data and previously published numerical predictions. The application to injection molding problems is done by using an ALE formulation. For the piston-driven flow, the ALE formulation is shown to provide similar results as an Eulerian approach on a fixed mesh, thus indicating that the procedure performs well. Application to the mold filling of a rectangular plate shows the ability to use this method to the solution of PIM.

REFERENCES

1. Karnis A, Mason SG. The flow of suspensions through tubes: VI. Meniscus effects. *Journal of Colloid and Interface Science* 1967; **23**:120–133.
2. Leighton D, Acrivos A. The shear-induced migration of particles in concentrated suspensions. *Journal of Fluid Mechanics* 1987; **181**:415–439.
3. Graham AL, Altobelli SA, Fukushima E, Mondy LA, Stephens TS. NMR imaging of shear-induced diffusion and structure in concentrated suspensions undergoing Couette flow. *Journal of Rheology* 1991; **35**:191–201.
4. Barrière T, Gelin JC, Liu B. Improving mould design and injection parameters in metal injection moulding by accurate 3D finite element simulation. *Journal of Material Processing Technology A* 2002; **125–126**:518–524.
5. Petera J, Kotynia M. The finite element model of non-isothermal semi-solid fluid flow. *Journal of Heat and Mass Transfer* 2004; **47**:1483–1498.
6. Manninen M, Taivassalo V. *On the Mixture Model for Multiphase Flow*, vol. 288. VTT Publications: Finland, 1996.
7. Pineau F, Ilinca F, Hétu J-F. A mixture approach for semisolid metal mold filling simulations. *Proceedings of MCWASP 2006*. TMS, Warrendale, PA, 2006; 1063–1070.
8. Phillips RJ, Armstrong RC, Brown RA, Graham AL, Abott JR. A constitutive equation for concentrated suspensions that accounts for shear-induced particle migration. *Physics of Fluids*, *A* 1992; **4**:30–40.

DOI: 10.1002/fld

9. Subia SR, Ingber MS, Mondy LA, Altobelli SA, Graham AL. Modelling of concentrated suspensions using a continuum constitutive equations. *Journal of Fluid Mechanics* 1998; **373**:193–219.
10. Tetlow N, Graham AL, Ingber MS, Subia SR, Mondy LA, Altobelli SA. Particle migration in a Couette apparatus: experiment and modeling. *Journal of Rheology* 1998; **42**(2):307–327.
11. Nott PR, Brady JF. Pressure driven flow of suspensions: simulation and theory. *Journal of Fluid Mechanics* 1994; **275**:157–199.
12. Morris JF, Boulay F. Curvilinear flows of noncolloidal suspensions: the role of normal stresses. *Journal of Rheology* 1999; **43**(5):1213–1237.
13. Fang Z, Mammoli AA, Brady JF, Ingber MS, Mondy LA, Graham AL. Flow-aligned tensor models for suspension flows. *International Journal of Multiphase Flow* 2002; **28**:137–166.
14. Lyon MK, Leal LG. An experimental study of the motion of concentrated suspensions in two-dimensional channel flow. Part 1. Monodisperse systems. *Journal of Fluid Mechanics* 1998; **363**:25–56.
15. Shapley NC, Brown RA, Armstrong RC. Evaluation of particle migration models based on laser Doppler velocimetry measurements in concentrated suspensions. *Journal of Rheology* 2004; **48**(2):255–279.
16. Ilinca F, Hétu J-F. Three-dimensional filling and post-filling simulation of polymer injection molding. *International Polymer Processing* 2001; **16**:291–301.
17. Moraczewski T, Tang H, Shapley NC. Flow of a concentrated suspension through an abrupt axisymmetric expansion measured by nuclear magnetic resonance imaging. *Journal of Rheology* 2005; **49**(6):1409–1428.
18. Wu S. Surface d interfacial tensions of polymers, oligomers, plasticizers and organic pigments. *Polymer Handbook*, Brandup J, Immergut EH, Grulke EA (eds). Wiley: New York, 1999; 521–541.
19. Krieger IM, Dougherty TJ. A mechanism for non-Newtonian flow in suspensions of rigid spheres. *Transactions of the Society of Rheology* 1959; **3**:137–152.
20. Ilinca F, Hétu J-F. Finite element solution of three-dimensional turbulent flows applied to mold-filling problems. *International Journal for Numerical Methods in Fluids* 2000; **34**:729–750.
21. Franca LP, Frey SL. Stabilized finite element methods: II. The incompressible Navier–Stokes equations. *Computer Methods in Applied Mechanics and Engineering* 1992; **99**:209–233.
22. Tezduyar TE, Shih R, Mittal S, Ray SE. Incompressible flow using stabilized bilinear and linear equal-order-interpolation velocity–pressure elements. *Research Report UMSI 90/165*, University of Minnesota/Supercomputer Institute, Minneapolis, 1990.
23. Ilinca F, Hétu J-F, Pelletier D. On stabilized finite element formulations for incompressible flows. *Thirteenth AIAA Computational Fluid Dynamics Conference*, Snowmass, Colorado, 1997; AIAA Paper 97-1863.
24. Zienkiewics OC, Zhu JZ. The superconvergent patch recovery and *a posteriori* error estimates. Part 1: the recovery technique. *International Journal for Numerical Methods in Engineering* 1992; **33**:1331–1364.
25. Ilinca F, Pelletier D, Garon A. An adaptive finite element method for a two-equation turbulence model in wall-bounded flows. *International Journal for Numerical Methods in Fluids* 1997; **24**:101–120.
26. Ilinca F, Hétu J-F. Three-dimensional finite element solution of gas-assisted injection moulding. *International Journal for Numerical Methods in Engineering* 2002; **53**:2003–2017.
27. Abbott JR, Tetlow N, Graham AL, Altobelli SA, Fukushima E, Mondy LA, Stephens TS. Experimental observations of particle migration in concentrated suspensions: Couette flow. *Journal of Rheology* 1991; **35**(5):773–795.
28. Seshadri V, Sutera SP. Concentration changes of suspensions of rigid spheres flowing through tubes. *Journal of Colloid and Interface Science* 1967; **27**:101–110.
29. Ramachandran A, Leighton Jr DT. The effect of gravity on the meniscus accumulation phenomenon in a tube. *Journal of Rheology* 2007; **51**(5):1073–1098.
30. Tang H, Grivas W, Homentcovschi D, Geer J, Singler T. Stability considerations associated with the meniscoid particle band at advancing interfaces in Hele–Shaw suspension flows. *Physical Review Letters* 2000; **85**:2112–2115.
31. Altobelli SA, Fukushima E, Mondy LA. Nuclear magnetic resonance imaging of particle migration in suspensions undergoing extrusion. *Journal of Rheology* 1997; **41**(5):1105–1115.